

## Pore-space percolation in sea ice single crystals

D. J. Pringle,<sup>1,2</sup> J. E. Miner,<sup>2</sup> H. Eicken,<sup>2</sup> K. M. Golden<sup>3</sup>

- 5 1. Arctic Region Supercomputing Center, University of Alaska Fairbanks, AK, USA
2. Geophysical Institute, University of Alaska Fairbanks, AK, USA
3. Department of Mathematics, University of Utah, Salt Lake City, UT, USA

E-mail: pringle@gi.alaska.edu

10

### ABSTRACT

We present imagery of sea ice microstructure obtained with x-ray computed tomography, and analyze critical behavior with a novel percolation-theory characterization of sea-ice thermal evolution. We studied single crystals between -18 °C and -3 °C and found arrays of near-parallel intra-crystalline brine layers, whose connectivity and complex morphology evolve with temperature. While percolation theory has been applied to disordered composite materials for fifty years, key variables such as the infinite cluster density, percolation probability, correlation length, and their critical exponents, have been computed only for lattice models. Here, as a potential first analysis of its kind for a natural material, we compute such functions from our 3-D imaging of the pore-space evolution. Using finite-size scaling analysis, we find anisotropic percolation thresholds with critical porosity  $p_{c,v} = 4.6 \pm 0.7$  % in the vertical, laterally  $p_{c,pll} = 9 \pm 2$  % parallel to the layers and  $p_{c,perp} = 14 \pm 4$  % perpendicular to them. We relate the microstructure's anisotropic critical behavior to previous measurements of anisotropy in bulk dc conductivity and fluid permeability. Our results are an important step towards realistic transport property models of sea ice, with implications for other frozen and granular materials.

30 0750 Cryosphere, Sea ice; 0770 Cryosphere, Properties; 5112 Physical Properties of Rocks, Microstructure; 5114 Physical Properties of Rocks, Permeability and porosity; 3299 Mathematical Geophysics, General or miscellaneous

## 1. INTRODUCTION

35

Sea ice is a dynamic porous medium due to the presence of brine inclusions whose volume fraction depends on temperature and bulk salinity. Brine is incorporated during growth as intra-crystalline layers and at grain boundaries [*Weeks and Ackley, 1986; Eicken, 2003*]. Inclusions shrink with cooling as brine salinity must increase to maintain thermohaline equilibrium with the surrounding ice, and vice-versa for warming. Brine porosity can exceed 70% at the ice-ocean interface [*Notz et al., 2008*] and approach zero in cold, desalinated multiyear ice [*Weeks and Ackley, 1986; Eicken, 2003*].

40

Comparatively little is known, however, about associated changes in inclusion morphology and pore-space connectivity. The present work is motivated by the dependence of sea ice properties on inclusion morphology and connectivity, and to gain insight into the processes governing pore space thermal evolution necessary to develop realistic predictive models of sea ice microstructure. Such questions are important since the microstructure controls bulk properties underpinning the large-scale behavior of sea ice, its role in earth's climate system, and as an important habitat for algal and bacterial communities [*Thomas and Dieckmann, 2003*].

45

50

Bulk properties of sea ice are sensitive to the anisotropy, number-density, connectedness, and temporal evolution of individual inclusions and secondary networks, and over a range of length scales. These properties and processes include remote sensing signatures [*Hallikainen and Winebrenner, 1992; Golden et al., 1998b, 1998c*], optical properties [*Light et al., 2003*], colonization of sea ice by microorganisms [*Krembs et al., 2000*] and pollutant transport [*Pfirman et al., 1995*]. Of special note is the fluid permeability which controls fluid flow in sea ice, affecting ice albedo through melt pond development [*Eicken et al., 2004*], nutrient delivery to microorganisms [*Krembs et al., 2000*] and salinity profile evolution [*Cox and Weeks, 1975; Weeks and Ackley, 1986; Wettlaufer et al., 2000; Vancoppenolle et al., 2007*].

55

60

Sea ice is essentially impermeable for brine volume fractions below 5%, above which permeability increases rapidly [*Cox and Weeks, 1975; Freitag, 1999; Freitag and Eicken, 2003; Eicken et al., 2004; Petrich et al., 2006*], inspiring initial applications of

65

percolation ideas to sea ice [Golden *et al.*, 1998a, 2007; Zhu *et al.*, 2006]. Golden *et al.* [1998a] equated sea ice brine volume fraction with porosity and explained with an excluded-volume model the apparent critical porosity for fluid permeability,  $p_c \approx 5\%$ . For a typical FY ice salinity of 5 ppt, this threshold corresponds to a critical temperature  
70 of approximately  $-5\text{ }^\circ\text{C}$ , dubbed the ‘rules of fives’ [Golden *et al.*, 1998a].

A detailed description of the thermal evolution of brine inclusions is lacking, and reflects several measurement challenges. Sample microstructure should not be disturbed during preparation and measurement, requiring careful thermal control. Inclusions show length  
75 scales from sub-mm brine layers to meter-long channels, requiring scale-specific methods which necessarily have optimal resolution over only some range of these length scales. Imaging methods should be free of stereological and resolution artifacts [Eicken *et al.*, 2000; Jerram and Higgins, 2007]. Inclusion statistics have been derived in several studies with thin section microscopy. Perovich and Gow [1996] reported brine inclusion  
80 number densities of 1.0 to 4.5 per  $\text{mm}^3$ . Light *et al.* [2003] resolved 24 pockets per  $\text{mm}^3$ , and a power law scaling of inclusion number density with length –highlighting the effect of imaging resolution. Cole and Shapiro [1988] described inclusion shapes that ranged from spherical to vertically elongated ellipsoids. Nevertheless, the limitations of thin section microscopy motivated the use of non-destructive tomography. Our work builds on  
85 the low-resolution x-ray tomography of Kawamura [1998] and later efforts by Lange [1988]. Eicken *et al.* [2000] used magnetic resonance imaging (MRI) to measure inclusion dimensions from 2D horizontal and vertical images of polycrystalline natural and tank-grown sea ice with a resolution of  $0.2 \times 0.2 \times 1\text{ mm}$ . They found an increase in inclusion length and elongation with warming, and good agreement with high-resolution  
90 thin section microscopy.

Constrained by the lack of pore evolution data, microstructural models of sea ice are highly simplified. The elongated brine channels and ice plate model of Assur [1960] remains the standard descriptive and engineering model for mechanical properties. An  
95 ellipsoidal inclusion model was later developed by Tinga [1973] and applied by Vant *et al.* [1978] to the dielectric permittivity of sea ice, with parameter fitting (vertical aspect ratio, and inclination angle) from measurements in the range 0.1 - 40 GHz. Effective

medium models for thermal properties have used spherical brine and air inclusions [Yen, 1981; Pringle *et al.*, 2007].

100

Percolation theory addresses transitions in disordered multi-component systems whose properties depend on component connectivity [e.g. Stauffer and Aharony, 1994; Bunde and Havlin, 1995; Christensen and Moloney, 2005]. Below a critical volume fraction  $p_c$  there are no percolating pathways spanning a sample, and properties near  $p_c$  show power law scaling related to  $(p-p_c)$ . In numerical lattice simulations, the volume fraction corresponds to the probability a site is occupied or a bond exists; in tomographic images it corresponds to porosity. Percolation theory has been used for 50 years to study a broad range of materials including rocks [Broadbent *et al.*, 1957; Bourbie and Zinszner, 1985; Fredrich *et al.*, 2006], semiconductors [Shklovskii and Efros, 1984], thin films [Davis *et al.*, 1991], glacial ice [Enting, 1985], polycrystalline metals [Chen and Schuh, 2007], radar absorbing coatings [Kusy and Turner, 1971], and carbon nanotube composites [Kirylyuk and van der Schoot, 2008]. For these materials it is generally difficult to vary the volume fraction of the phase whose connectivity controls bulk properties, e.g. in rocks one must analyze different samples [Bourbie and Zinszner, 1985; Fredrich *et al.*, 2006]. For sea ice, varying temperature results in relatively large changes in porosity, enabling us to compute percolation functions from the thermal evolution of individual samples' microstructure. We believe these to be the first such calculations of key percolation theory functions from the evolving pores space of a natural material.

105

110

120

125

Here we give a detailed, quantitative description of sea ice microstructure and its critical behavior with temperature. We have grown sea-ice single crystals – the building blocks of polycrystalline sea ice – and imaged the thermal evolution of their complex pore space with x-ray computed tomography. We characterize the structure by computing key functions of classical percolation theory. Using finite-size scaling and known universal critical exponents, we estimate anisotropic percolation thresholds for preferentially vertical near-parallel brine layers connected by occasional necks. We discuss up-scaling our results to explain anisotropic bulk transport properties, as well as future work with x-ray imaging of sea ice, and implications for other frozen and granular materials.

130

## 2. METHODS

### 2.1 Single crystal sample preparation

135 Large single crystals of artificial sea ice were grown in a temperature-controlled cold room. Saline solutions were seeded with oriented single crystals of freshwater ice, following the method described by *Kawamura* [1986]. Blocks of fresh water ice up to 50 cm to a side and comprising decimeter-sized crystals, were extracted from a local gravel pit in Fairbanks, Alaska. Following determination of crystal-optical alignment with a

140 universal stage, 1-2 cm thick seed plates with horizontal c-axes were cut. Ice was grown at  $-8\text{ }^{\circ}\text{C}$  from solutions of 50:50 % by weight InstantOcean<sup>TM</sup> artificial sea salt and x-ray contrast agent CsCl. Solutions were cooled close to their freezing point and the seed plate lowered onto their upper surface as a substrate for oriented ice growth. Universal stage analysis showed excellent crystallographic alignment in samples as large as  $40 \times 20 \times 10$

145 cm. Tomography samples were prepared inside a cold room at  $-20\text{ }^{\circ}\text{C}$ , a sufficiently low temperature to inhibit brine drainage from the ice. Large single crystals were cut into several sections and turned down with a lathe until they fit tightly into 3 cm diameter, 3 cm-tall, low-density polyethylene (LDPE) cylindrical sample holders. Bulk salinity and density profiles were obtained from parallel samples with a YSI 30 salinometer.

150

### 2.2 X-ray Computed Tomography

X-ray measurements were performed with a Skyscan 1074 fan-beam x-ray source micro-CT scanner, in a temperature-controlled sub-chamber of the cold room in which the

155 samples were grown and prepared. These measurements return a 3D image of x-ray absorption. The LDPE cylindrical sample holders were mounted on a stage and rotated about the vertical axis, with an x-ray absorption image taken at each  $1^{\circ}$  step . Data were output as a serial stack of  $736 \times 736$  pixel, 8-bit bitmap images of x-ray absorption with ‘CT’ numbers in the range 0-255. Using the maximum available sample size gave cubic

160 voxels  $41.5\text{ }\mu\text{m}$  to a side. See Figure 1.

[ FIGURE 1 ]

Images were acquired with the highest available energy, 40 keV ( $\lambda = 0.31 \text{ \AA}$ ) and current  
 165 (1mA) to reduce acquisition time. Resolution was maximized with an exposure time of  
 670 ms and each acquisition averaged over 8 repeat frames to reduce noise from external  
 sources. A sequence of measurements was performed at different temperatures on  
 individual samples without removal from the sample holder housed inside the scanner.  
 Samples were cooled to  $-25 \text{ }^\circ\text{C}$ , and successive measurements made at  $-18 \text{ }^\circ\text{C}$ ,  $-15 \text{ }^\circ\text{C}$ , -  
 170  $12 \text{ }^\circ\text{C}$ ,  $-8 \text{ }^\circ\text{C}$ ,  $-7 \text{ }^\circ\text{C}$ ,  $-6 \text{ }^\circ\text{C}$ ,  $-5 \text{ }^\circ\text{C}$ ,  $-4 \text{ }^\circ\text{C}$ , and  $-3 \text{ }^\circ\text{C}$ .

### 2.3 Image Processing and Segmentation

We segmented the x-ray images with each voxel designated as either ice, brine or air.  
 175 The porosity is the combined volume of air and brine voxels. We applied a 3x3 median  
 filter to each slice to reduce noise with minimal edge loss, averaged vertically over 3  
 slices, and applied radial detrending. Air volumes typically less than 0.1% were formed  
 by occasional brine movement. We identified a global CT threshold for air by fitting  
 double Gaussian peaks to manually chosen sub-volumes with ice and air inclusions, but  
 180 no brine inclusions. To segment brine from ice we exploited the known phase relation  
 for sea ice, adapted to the InstantOcean<sup>TM</sup>-CsCl-H<sub>2</sub>O system. This was necessary because  
 ice and brine have a density contrast of only 20%. Even at the relatively low energy of 40  
 keV, the contrast due to the addition of high-atomic-number Cs was useful, but  
 insufficient to unambiguously segment ice and brine for our dynamic range. The phase  
 185 behavior of sea ice allows calculation of brine volume fraction from temperature  $T$ , bulk  
 salinity  $S$ , and density  $\rho$ . We adapted the equations of *Weeks and Cox* [1983] and  
*Leppäranta and Manninen* [1988] to the InstantOcean<sup>TM</sup>-CsCl-H<sub>2</sub>O system using the  
 freezing-point depression for the combined system (see Appendix).

190 Brine was segmented from ice with global thresholding such that the volume fraction of  
 brine (plus the small contribution from air) matched the target porosity calculated from  $T$ ,  
 $S$  and  $\rho$ . An exact match is not possible with integer thresholding, so we found the integer  
 thresholds  $CT$  and  $CT + 1$  giving porosities immediately above and below the target

porosity. We processed in parallel the segmented data sets with these porosities and  
195 calculated final results by interpolation to the target porosity (see Table 1). Constrained  
by the known freezing-point depression for our samples, this interpolation improved the  
resolution of our segmentation beyond that possible for un-guided thresholding.

The structure of the brine pore space is seen in isosurface plots in Figure 1. Plots for -18  
200 °C, -8 °C and -4 °C, show the pore-space evolution as porosity changes from 2.2 to 4.6  
to 8.8 %. To more clearly show the structure, these are  $50 \times 50 \times 200$  voxel sub-volumes,  
and they are close to being collocated. The upper images clearly show near-parallel  
layering, but overall we see a pore space much more complicated than simple models  
suggest. These figures illustrate aspects of the critical behavior analyzed below. At  $p =$   
205 2.2 % we see many disconnected inclusions, and there is no vertically percolating path.  
At  $p = 8.8$  %, there are shunts, or ‘necks’, connecting the layers, and the pore space is  
well connected from top to bottom. At  $p = 4.6$  %, very close to the vertical percolation  
threshold computed below, the layers are vertically elongated with only a few necks. The  
lower figures show a side-on view of the layers, with images rotated by  $90^\circ$ . Again, we  
210 see connectivity increasing with porosity as the pore space changes from isolated  
inclusions to extended, near-parallel layers. The lateral connectivity appears higher along  
the layers (lower plots) than across them (upper plots). In fact  $p = 8.8\%$  is close to the  
lateral connectivity threshold we find parallel to the layers, whereas the threshold across  
the layers is higher still.

215

#### 2.4 Pore space analysis with 3DMA

For the connectivity analysis of our 3D tomographic images, we used the freely-available  
3DMA software package. 3DMA-Rock (3-Dimensional Medial Axis) is a modular  
220 research code which has been previously applied to a variety of porous media for pore-  
space characterization and single- and two-phase pore-fluid displacement [e.g. *Lindquist*,  
1999; *Prodanović et al.*, 2006]. The medial axis of a digitized object is a centrally-located  
skeleton which preserves the original topology and geometry of the object [*Lindquist*,  
1999]. We use 3DMA to compute pore space connectivity, using the 26-connected

225 medial axis as a search path. Here ‘26-connected’ means that adjacent voxels on the medial-axis can connect at any of the 26 corners, edges or faces of a voxel.

As a comment on nomenclature, porous media microstructure is generally described in terms of ‘pores’ connected by ‘throats’. Throats are local restrictions in the pore space, and control drainage, whereas pores control imbibition [e.g. *Hunt, 2005*]. Previous  
 230 characterization of sea ice microstructure has focused on the length and size of discrete ‘brine inclusions’, neglecting the role of throats within these inclusions.

## 235 **2.5 Key functions of percolation theory**

Our tomographic images of brine and ice voxels are similar to 3D site percolation lattices [e.g. *Stauffer and Aharony, 1994; Bunde and Havlin, 1995; Christensen and Moloney, 2005*], with sea ice porosity analogous to lattice site occupancy probability. Figure 2  
 240 illustrates the behavior of three percolation functions central to our work.

[ FIGURE 2 ]

The correlation function is the probability that two points separated by  $r$  are connected  
 245 through the phase of interest - in our case, the pore space. When  $r$  is large (see next paragraph), the two-point correlation function behaves as

$$g(r) \sim \exp(-r/\xi) \quad , \quad (1)$$

250 where  $\xi$  is the correlation length. In site percolation  $\xi$  is the mean distance between two sites on the same finite cluster , and is given by

$$\xi(p) \sim |p - p_c|^{-\nu} \quad . \quad (2)$$

255 where  $\nu$  is the correlation length critical exponent, which has a universal value depending  
 only on the system dimension, and  $\nu = 0.876$  in 3D [*Bunde and Havlin, 1995*]. We do not  
 consider the correlation length above  $p_c$  as here it is defined for the matrix phase, in our  
 case ice. The criterion above that ‘ $r$  is large’ is that  $r > \xi$ , which is satisfied for our low  
 porosity samples for which the correlation length is small, and we do observe exponential  
 260 behavior.

The order parameter  $P_\infty(p)$  is also known as the ‘infinite cluster density’ in infinite  
 samples. It is the probability that any randomly chosen position is on a percolating path.  
 For  $p < p_c$ ,  $P_\infty(p) = 0$ , and  $P_\infty(p) = 1$  only at  $p = 1$ . See Figure 2. As  $p$  approaches  $p_c$   
 265 from above,  $P_\infty(p)$  vanishes as

$$P_\infty(p) \sim (p - p_c)^\beta \quad . \quad (3)$$

Here  $\beta$  is also a universal exponent, with  $\beta = 0.418$  in 3D [*Bunde and Havlin, 1995*]. The  
 270 percolation probability  $\Pi(p)$  is the probability there exists a percolating path across a  
 sample. For an infinite lattice,  $\Pi(p)$  is a step function with  $\Pi(p < p_c) = 0$  and  $\Pi(p > p_c) =$   
 1.

Figure 2 shows the behavior of these quantities in infinite samples, for which they are  
 275 defined, and for finite samples in which we are interested. Their behavior in finite systems at  
 $p = p_c$  is described by finite-size scaling. The correlation length  $\xi$  diverges at  $p_c$  and is  
 therefore always greater than the system size  $L$ . This leads to properties related to  $p_c$   
 showing power-law scaling with  $L$  [e.g. *Stauffer and Aharony, 1994; Bunde and Havlin,*  
*1995; Christensen and Moloney, 2005*]. We use finite size scaling to compute the  
 280 intrinsic, anisotropic infinite-sample thresholds of our samples.

### 3 COMPUTATIONAL RESULTS AND ANALYSIS

285 We have analyzed the connectivity of the pore-space as a whole using 3DMA. Input was a series of x-ray tomography image stacks from a single-crystal sample processed as above and imaged between  $-18\text{ }^{\circ}\text{C}$  and  $-3\text{ }^{\circ}\text{C}$ . We analyzed this sample over a 7.5 mm thickness with a constant salinity  $S = 9.4 \pm 0.5$  ppt.

290 Using 3DMA, we have calculated the vertical correlation length as a function of porosity and have used finite-size scaling to calculate anisotropic percolation thresholds. We computed the fractional connectivity  $f$  between opposite faces in cuboid volumes. This is the fraction of medial axis voxels on the start face which are connected via a percolating medial axis path to the opposite end face (see Figure 1a). The fractional connectivity is a  
 295 measure of whether there is at least one spanning path from each start voxel, and is insensitive to the number and properties of these paths.

#### 3.1 Correlation length and connectivity depth-dependence

300 We have derived the porosity dependence of the correlation length in the vertical direction from the depth-dependence of the fractional connectivity. Using cuboid samples with horizontal extent  $380 \times 380$  voxels, we computed the fractional connectivity over increasing depths, from the surface to a maximum depth of  $z = 180$  voxels. From equation (2.5), we expect an exponential decay in  $f(z)$  when the correlation  
 305 length is smaller than the sample depth, and Figure 3a shows that we see this at low porosities. The fitted lines are of the form:  $f = C \exp(-z/z_0)$ , where  $C$  is a constant and  $z_0$  a penetration depth. At high porosities we do not expect exponential behavior because for  $p > p_c$  the correlation length is related to the ice phase not the pore space. In fact we found power-law behavior for  $p > 7\%$  with good fits of the form  $f = k z^\alpha$ , where  $k$  is a  
 310 constant.

[ FIGURE 3 ]

The fitted values of  $z_0$  for  $p < p_c$  correspond to a vertical correlation length  $\xi_V$  as in  
 315 equation (1) for connections between two parallel planes. We will see that the connecting  
 pathways are preferentially vertical, so that multiplying the fractional connectivity by the  
 porosity approximates well the two-point correlation function in the vertical direction.  
 This multiplication does not affect the fitted penetration depths  $z_0$  in Figure 3a, only the  
 pre-factors  $C$ . Figure 3b shows the fitted  $z_0$  values for  $p \leq 6\%$ . In an infinite domain,  $\xi$   
 320 diverges as  $p$  increases towards  $p_c$ . It is bounded by the sample size in a finite system, and  
 Figure 3b shows  $z_0$  to be approaching the sample size  $L = 180$  voxels for  $p \approx 6\%$ . In the  
 absence of analytical results for  $\xi(p)$  in finite systems, we are unable to extrapolate to the  
 intrinsic threshold. However we have computed  $p_c$  using finite scaling, which we now  
 describe [Christensen and Moloney, 2005].

325

### 3.2 Percolation thresholds from finite-size scaling

We used finite-size scaling to compute the vertical percolation threshold with four  
 methods, whose weighted mean gives  $p_{c,v} = 4.6 \pm 0.7\%$ , slightly lower than the bulk fluid  
 330 permeability threshold. We computed the connectivity for ensembles of cubic sub-  
 volumes with side lengths  $L = 50, 75, 100, 125, 150$  and  $180$  voxels, positioned in a  
 (pseudo-)random fashion [Matsumoto and Nishimura, 1998] excluding boundaries. See  
 Figure 1. The number of sub-volumes was scaled as  $N_L \propto L^{-3}$  to hold constant the total  
 volume sampled at each length scales. From each ensemble we computed the finite-size  
 335 versions of the percolation probability  $\Pi$  and the order parameter  $P_\infty$ .

$\Pi(p, L)$  is the probability of a percolating pathway across a sample of porosity  $p$  and size  
 $L$  [Christensen and Moloney, 2005]. We compute  $\Pi(p, L)$  as the fraction of sub-volumes  
 with one or more percolating paths in each ensemble [Biswal et al., 1998]. For an infinite  
 340 sample,  $\Pi(p)$  is a step function with  $\Pi(p < p_c) = 0$  and  $\Pi(p > p_c) = 1$ . This transition  
 widens as sample size decreases. As seen in Figure 4a, the porosity range of our samples  
 is wide enough to cover the full transition from  $\Pi(p, L) = 0$  to  $1$  when  $L = 180$ , but not for  
 smaller length scales.

345 [ FIGURE 4 ]

We have found three estimates of the vertical threshold  $p_{c,v}$  from the finite-size scaling of  $\Pi(p, L)$ . To improve our porosity resolution we analyzed smooth curves fit to our data in Figure 4a, with the upper and lower curves used for uncertainty analysis. These curves  
 350 are all smooth interpolations because although scaling results exist at  $p_c$ , there are no analytical results for the full curves.

We first estimate  $p_c$  from the scaling of  $\Pi(p, L)$  with respect to  $L$ . When  $p = p_c$ , this is given by

355

$$\Pi(p_c, L) \propto L^{-\beta/\nu} \quad , \quad (8)$$

with  $\nu$  and  $\beta$  as in section 2.5 [Aharony and Stauffer, 1994; Christensen and Moloney, 1995]. Equation (8) implies that at  $p_c$  a log-log plot of  $\Pi(p, L)$  against  $L$  is linear with a  
 360 gradient  $m(L)$  given by

$$m(L) = \left. \frac{d(\log \Pi)}{d(\log L)} \right|_{p_c} = -\beta/\nu \quad . \quad (9)$$

Therefore  $p_c$  can be found as the porosity for which  $m(L) = -\beta/\nu = -0.477$ . Figure 4b  
 365 shows  $m(L)$  calculated from the smooth curves in Figure 4a. Interpolating between points adjacent to the target value  $m(L) = -0.477$  gives  $p_{c,\Pi} = 3.9 \pm 0.3$  %. Standard errors in  $m(L)$  come from weighted linear least squares fits using uncertainties from the outer curves in Figure 4a [Krystek and Anton, 2007]. We observe several percolation features in Figure 4b. For porosities both much smaller and much larger than  $p_{c,\Pi}$  we find  $m(L)$   
 370 approaching 0. We expect  $m(L) = 0$  for both  $p = 0$  and 1 because percolation cannot occur for any value of  $L$  at  $p = 0$ , and percolation occurs for all  $L$  at  $p = 1$ . For  $p$  between 0 and the transition region,  $m(L)$  is negative because smaller samples admit an increasing chance of percolation below the infinite-sample threshold. Similarly, between the

transition region and  $p = 1$ ,  $m(L)$  is positive since smaller samples also admit an  
 375 increasing chance of no percolation above  $p_c$ .

We found two further estimates of  $p_c$  from the  $\Pi(p,L)$  curves in Figure 4a. The point of  
 inflection  $p_{max}$  of these curves converges to  $p_c$  as [Stauffer and Aharony, 1994]:

$$380 \quad (p_{max} - p_c) \propto L^{-1/\nu} \quad . \quad (5)$$

From the curves in Figure 4a, we have numerically calculated  $d\Pi/dp$  and found  $p_{max}(L)$  as  
 the porosity with maximum  $d\Pi/dp$ . Figure 4c shows plots of  $p_{max}$  vs.  $L^{-1/\nu}$ , where  
 uncertainties give the range in  $p_{max}$  derived from the dashed curves in Figure 4a. As  $L$   
 385 increases,  $L^{-1/\nu}$  decreases so the value of  $p_c$  for the infinite size limit is given by the  
 vertical axis intercept. A weighted linear least-squares fit gives an intercept of  $p_{c,max} =$   
 $4.54 \pm 0.23$  %. The uncertainty here is the least squares estimate of the intercept standard  
 error [Krystek and Anton, 2007].

390 Similar scaling is displayed by  $p_{av}$ , the average porosity at which a percolating cluster  
 appears for the first time. This is given by [Stauffer and Aharony, 1994]:

$$p_{av} = \int_0^1 p \left( \frac{d\Pi}{dp} \right) dp \quad . \quad (6)$$

395 The special case of  $\Pi(p,L)$  being symmetric is not met for our data, so  $p_{av}$  scales as for  
 $p_{max}$ : [Stauffer and Aharony, 1994]:

$$(p_{av} - p_c) \propto L^{-1/\nu} \quad . \quad (7)$$

400 Values of  $p_{av}$  calculated with equation (6) are plotted against  $L^{-1/\nu}$  in Figure 4d. A least-  
 squares fit here gives an intercept of  $p_{c,av} = 5.14 \pm 0.44$  %. Uncertainties are as for  $p_{max}$   
 above.

$P_\infty(p, L)$  is the finite-size order parameter. In our case, this is the probability that any  
 405 voxel is connected through the brine phase to both the top and bottom of the sample.  
 Figure 5a shows ensemble average values for  $P_\infty(p, L)$  found with a burn algorithm to  
 compute the volume fraction of brine contained in the spanning paths.

[ FIGURE 5 ]

410

Figure 5a shows the resulting plots of  $P_\infty(p, L)$  against porosity for each length scale. As  
 in Figure 4a, the points are computed values, and the lines smooth interpolations used in  
 our analysis. We resolve only a small portion of the  $P_\infty$  curves, which, as shown in  
 Figure 2, reach  $P_\infty = 1$  only at  $p = 1$ . We see an increase with  $L$  in the porosity at which  
 415  $P_\infty$  becomes non-zero. This is expected because with decreasing sample size, the  
 appearance of the first percolating path becomes increasingly probable below  $p_c$

We have calculated  $p_c$  from the scaling of  $P_\infty(p, L)$  with  $L$ , which is the same as for  $\Pi(p,$   
 $L)$ :

420

$$P_\infty(p_c, L) \propto L^{-\beta/\nu} \quad . \quad (10)$$

Figure 5b shows results from the same log-log scaling analysis applied above to  $\Pi(p, L)$ ,  
 now expressed in terms of  $n(L)$ :

425

$$n(L) = \left. \frac{d(\log P_\infty)}{d(\log L)} \right|_{p_c} = -\beta/\nu \quad . \quad (9)$$

Interpolating between points adjacent to the target value  $n(L) = -0.477$  gives  $p_{c,PL} = 6.9 \pm$   
 0.7 %. Numerical simulations in fact suggest that this method may overestimate  $p_c$ .

430 *Christensen and Moloney* [2005] show that the scaling of  $P_\infty(p_c, L)$  for 2D site  
 percolation obeys equation (9) only for  $L$  greater than about 100. For  $L$  between 10 – 100,  
 their results suggest the power-law exponent is about twice  $-\beta/\nu$ . We don't necessarily

expect this result to apply to our system, due to differences with 2D site percolation.

Nevertheless, if we revise our target scaling to  $m(L) = -2\beta/\nu = -0.954$ , we find  $p_c = 5.3 \pm$   
 435 0.7 %, closer to the other estimates above.

Finite-size widening of the transition means we do not observe the classic percolation  
 result that in an infinite-sample the gradient  $dP_\infty/dp$  diverges at  $p_c$ . We are not aware of  
 any scaling results for the widening of this transition for finite samples. Indeed a  
 440 numerical simulations with  $L = 5000$  show the scaling predicted by equation (2) holds  
 only very close to the critical porosity, i.e.  $(p - p_c) \approx 10^{-2}$  [Christensen and Moloney,  
 2005].

Our measurements have better resolved the percolation probability  $\Pi$  than the order  
 445 parameter  $P_\infty$ . From a percolation theory point of view,  $P_\infty$  is more fundamental.  
 However,  $\Pi$  is in fact a more useful descriptor of pore-space geometry, as it relates  
 directly to the brine phase connectivity to which transport properties and processes are  
 sensitive.

### 450 **3.3 Percolation anisotropy**

We determined anisotropic horizontal thresholds with a similar analysis. The mean  
 horizontal orientation of brine layers was computed at each temperature using the  
 Quant3D code [Ketcham and Ryan, 2004; Ketcham, 2005], and the 3D image stacks  
 455 rotated to align this direction with the y-axis. To minimize the effect of image rotation on  
 our analysis, we in fact rotated the raw output and then reapplied the pre-processing and  
 segmentation. We then computed the ‘parallel connectivity’ along the brine layers, and  
 the ‘perpendicular connectivity’ across the layers. See Figure 1.

460 [ FIGURE 6 ]

We found a marked horizontal anisotropy in the percolation probability parallel to the  
 layers ( $\Pi_{pll}$ ) and perpendicular to them ( $\Pi_{perp}$ ). In contrast to  $\Pi$  in the vertical, our

porosity range does not span the critical transition regions for lateral connectivity and we  
 465 resolve only partial curves for  $\Pi_{pll}$  and  $\Pi_{perp}$ . Results in Figure 6a suggest threshold  
 behavior with a higher critical porosity for  $\Pi_{perp}$  than for  $\Pi_{pll}$ , with both being higher  
 than in the vertical. The transition width for  $\Pi_{pll}$  is also larger than in the vertical. These  
 differences attest to the different geometry in the pore-space connectivity as expected  
 from the images in Figure 1c. We attribute the horizontal anisotropy to the role of the  
 470 small necks between adjacent near-parallel brine layers. Connectivity perpendicular to  
 the layers is critically dependent on the presence of these connections. With increasing  
 porosity,  $\Pi_{perp}$  becomes non-zero not until  $p \approx 8\%$ . Connectivity along the brine layers is  
 enhanced by these necks, but is less dependent on them, and  $\Pi_{pll}$  is non-zero already by  $p$   
 $\approx 5\%$ . This point is illustrated in Figure 1c in which all samples show a higher degree of  
 475 connectedness along the brine layers (left-to-right in the lower images) than across the  
 (upper images).

We have not resolved enough of the  $\Pi_{pll}$  and  $\Pi_{perp}$  curves to repeat the finite scaling  
 analysis applied above to  $\Pi$ . Instead, we found thresholds  $p_{c,pll}$  and  $p_{c,perp}$  using simple  
 480 scaling arguments to map the partial curves of  $\Pi_{perp}(p)$  and  $\Pi_{pll}(p)$  to the  $\Pi(p)$  curves in  
 Figure 4a. Mapping by translation and dilation (Figure 6b) gave consistent results, with  
 means  $p_{c,pll} = 9 \pm 2 \%$  and  $p_{c,perp} = 14 \pm 4 \%$ . Uncertainties here reflect the scatter in  
 Figure 6a in the small number of laterally-percolating paths as well as the two scaling  
 approaches. In the case of  $L = 150$  and  $180$ , this is compounded by the increasing overlap  
 485 between ensemble sub-volumes.

We have derived our threshold estimates from the porosity range spanned by imaging the  
 same sample at increasing temperatures. We can therefore understand any non-monotonic  
 connectivity variations as non-physical. Our connectivity analysis is dependent on the  
 490 resolution (or not) of narrow throats. As in all porous media analysis of tomographic  
 images, we are ultimately limited by voxel resolution and segmentation accuracy  
 [Fredrich *et al.* 2006; Jerram and Higgins, 2007]. However, by analyzing the smooth  
 interpolated curves fit to our computed values of  $\Pi$  and  $P_\infty$ , we are here able to smooth  
 over variations caused by non-systematic processing artifacts.

495

## 4. DISCUSSION

### 4.1 Connection with bulk sea ice properties

500 Our vertical and horizontal single-crystal thresholds can explain larger-scale measurements, and inform microscopic modeling. Our vertical threshold  $p_c = 4.6 \pm 0.7 \%$  is only slightly smaller than the bulk permeability threshold of 5 % reported by *Cox and Weeks* [1975] from whose data a slightly modified re-analysis by *Petrich et al.* [2006] found  $p_c = 5.4\%$ . Fluid permeabilities 10-100 times larger in the vertical than the

505 horizontal have been reported, with up to almost an order of magnitude anisotropy in the horizontal components [*Freitag*, 1999]. In light of our results, we explain the latter by the limited connectivity provided by necks between parallel brine layers. While such lateral connections have been observed anecdotally in sea-ice thin sections [*Cole et al.*, 2002], it is not clear what controls their formation and growth.

510

Recent cross borehole dc-resistivity tomography in landfast FY ice revealed an increase in horizontal conductivity above a brine volume fraction  $p \approx 8 - 10 \%$  [*Ingham et al.*, 2008] and a vertical conductivity persisting to at least as low as  $p \approx 2 \%$  [*Ingham, M.*, personal communication, 2008]. At low  $p$ , the horizontal conductivity scaled as for

515 Archie's Law, with  $\sigma_H = \sigma_b p^m$ , where  $\sigma_b$  is the brine conductivity and  $m = 2.88$  [*Ingham et al.*, 2008]. However, with  $p > 8 - 10 \%$  the conductivity increased more strongly than predicted by Archie's Law, indicating a transition in the brine connectivity.

These bulk properties can be reconciled with our single crystal thresholds using a dual-

520 porosity conceptual model for polycrystalline columnar ice. Such ice has vertically elongated single crystals described by our results, with larger brine features present on grain boundaries and through secondary channels, all of which are preferentially vertical [*Weeks and Ackley*, 1986; *Eicken*, 2003]. The fluid permeability is limited by flow-path restrictions but the dc conductivity is not, and whereas the permeability is a measure of

525 the connectivity of larger-diameter brine features, the conductivity is sensitive also to

small scale connectivity. At sufficiently low porosity, the larger features disconnect from each other, but are weakly connected by intra-crystalline brine layers. The probability of a connecting pathway, as measured by  $\Pi(p,L)$ , is non-zero for finite-sized samples even below the bulk threshold. Such micrometer-scale brine layer connections would give a finite conductivity but strongly limit the fluid permeability. This dual porosity model is anisotropic through both the single crystal anisotropy we have measured, and the preferential vertical orientation and connectivity of larger brine features indicated by the permeability anisotropy. Therefore, just as the horizontal connectivity in single crystal samples is limited by necks between layers, the dm-scale horizontal conductivity is limited by single crystal connections between larger brine drainage features.

To pursue these connections further, it would be useful to make similar measurements to assess differences due to variations in growth rate and therefore mean inter-lamellar spacing [e.g. *Nakawo and Sinha*, 1984]. Analysis of polycrystalline samples may enable separation of connectivity contributions from intra- and inter-crystalline brine, allowing quantitative development of a dual-porosity sea ice microstructure model. Measurements over repeat temperature cycling of carefully collocated samples would provide direct insight into the mechanisms driving thermal evolution of individual pores and throats [e.g. *Eicken et al.*, 2000]. A resolution improvement of an order of magnitude or more may be achieved with synchrotron measurements. Further to microstructural analysis, the 3D structures returned by high-resolution tomography may be used as domains for lattice Boltzmann modeling to compute permeability and study oil-water-ice interaction. Similar approaches have been applied to firn [*Freitag et al.*, 2002] and sandstones [e.g. *Fredrich et al.*, 2006]. Likewise, the microstructure may also be used as a domain for heat transfer and thermal evolution calculations, as applied to snow by *Kaempfer et al.* [2005].

## 4.2 Broader implications for frozen and granular materials

Low-temperature connectivity and its associated length scales are of great importance for the role of sea ice and other impurity-laden ice bodies like permafrost as microbial habitats. The percolation probability curves in Figure 4a indicate that even at low porosities (corresponding to temperatures well below  $-10\text{ }^{\circ}\text{C}$ ), significant fluid exchange

may be sustained at length scales relevant for microbial processes in cold environments [Deming and Eicken, 2007]. The results presented here provide the first quantitative  
560 evidence of potential microstructural constraints on biological activity and genetic segregation in frozen materials. Moreover, the finite-size scaling analysis yields information on the temperature dependence of the length scales governing transport of nutrients and biogenic particulates in frozen media such as sea ice.

565 While we only consider columnar sea-ice crystals, our work has greatly extended previous microstructural models [Assur, 1960; Vant, 1978; Golden *et al.*, 1998a] which were not or only marginally able to capture several key aspects of sea-ice transport properties and their temperature dependence. Sea ice may serve as a high-homologous temperature analog in the study of a range of other materials in the solar system. The  
570 present findings shed light on a system that exhibits microstructural controls on porous fluid transport hypothesized for mantle and crustal materials [Wark *et al.*, 2003; Roberts *et al.* 2007]. Melt percolation is debated mechanism for planetary core formation, support for which has come from recent synchrotron imaging of synthetic olivine-iron-sulfide partial melt samples used for permeability computations with lattice Boltzmann modeling  
575 [Roberts *et al.*, 2007].

The microstructural controls on pore-space morphology within the brine layers evident in Figure 1 remain to be explored in more depth. The data do demonstrate, however, that for ordered arrays of intra-crystalline inclusions common in a range of artificial and  
580 geomaterials, anisotropy can account for as much as a factor three difference in the magnitude of the critical porosity. Due to its differential impact on electric and fluid transport properties, this anisotropy in  $p_c$  may be of relevance both as a diagnostic of microstructural evolution and a controlling factor in transport through anisotropic media.

585

## 5. CONCLUSIONS

Our measurements and percolation theory analysis have shown that x-ray computed tomography and a porous medium approach can improve our understanding of the

590 relatively poorly known pore-space evolution of sea ice. Our new results for anisotropic percolation thresholds in sea ice single crystals provide a basis to understand anisotropic bulk transport properties, and we have found length-scales for brine connectivity relevant to nutrient delivery and other processes. Pore space images illustrate the arrays of vertically-elongated near-parallel layers and occasional necks between them which  
595 underlie the percolation anisotropy. Key to accurate pore space imaging and analysis are optimizing resolution and image segmentation. The use of an x-ray contrast agent and exploiting the phase behavior of doped sea ice were central to our measurements in this regard. Our work shows the way for - and suggests - follow up work towards the ultimate goal of developing quantitative models of sea ice microstructure and its thermal  
600 evolution.

Much may be gained from higher resolution (e.g. synchrotron) measurements to enable further porous medium analysis of pore and throat size distributions and critical pathway analysis, and to provide domains for transport modeling. Measurements on  
605 polycrystalline samples may allow separation of the roles of intra-crystalline brine inclusions, and larger features including along grain boundaries. Some of this work is in progress. Many of these methods are mature in the study of other porous media [e.g. *Prodanović et al.*, 2006; *Fredrich et al.*, 2006; *Jerram et al.*, 2007] making multi-disciplinary work attractive for further advances to understand sea ice microstructure. A  
610 key point in this regard will be to identify the pore-space parameters most relevant to different sea ice process and transport studies, and to translate between these and parameters of interest in other porous media for which results and computational methods already exist.

615 Sea ice has a dynamic porosity ranging over wide length scales. It is easily controlled by varying temperature, making sea ice not only a fascinating porous medium in its own right but also providing an analog for other frozen and granular materials. Factors motivating further improvements in understanding sea ice microstructure include its climatic, environmental and biological interactions. As in our novel percolation theory  
620 analysis, there is potential for - and benefit from - the new application of theoretical models and analyses.

**Acknowledgements**

625

We thank Maša Prodanović, contributing developer and code maintainer for 3DMA; Richard Ketcham, developer of Quant3D; Don Bahls for technical support, and Miho Aoki for visualizations. For weighted least squares fits for data with uncertainties we used code developed and freely distributed by Mathias Anton. This research used

630

computational resources at the Arctic Region Supercomputing Center, and was supported by the US National Science Foundation Division of Atmospheric Sciences and Division of Mathematical Sciences.

## References

- 635 Assur, A. (1960), Composition of sea ice and its tensile strength, CRREL Report, 44, U.S. Army Cold region Research and Engineering Laboratory, Hanover, NH.
- Biswal, B., C. Manwart, and D. Hilfer (1998), Three dimensional local porosity analysis of porous media. *Physica A*, 255, 221.
- Bourbie, T., and B. Zinszner (1985), Hydraulic and acoustic properties as a function of  
640 porosity in Fontainebleau sandstone. *J. Geophys. Res.*, 90, 1524–1532.
- Broadbent, S. R., and J. M. Hammersley (1957), Percolation processes. I: Crystals and mazes, *Proc. Cambridge Philos. Soc.*, 53, 629-641.
- Bunde, A., and S. Havlin (1995), Percolation I, in *Fractals and Disordered Systems*, edited by A. Bunde and S. Havlin, pp.59-114, Springer, Berlin.
- 645 Chen, Y., and C. A. Schuh (2007), Percolation of diffusional creep: A new universality class. *Phys. Rev. Lett.* 98, 035701.
- Christensen, K., and N. R. Moloney (2005) *Complexity and Criticality*, Imperial College Press, London.
- Cole, D. M. , and L. H. Shapiro (1998), Observations of brine drainage networks and  
650 microstructure of first-year sea ice. *J. Geophys. Res.*, 103(C10), 21739–21750.
- Cole, D. M., H. Eicken, L. H. Shapiro, and K. Frey (2002), Some observations of high porosity layers and brine drainage features in first-year sea ice, Proceedings of the 16th IAHR International Symposium on Ice: Ice in the Environment, Dunedin, New Zealand, 2nd-6th Dec. 2002, vol. 2, 179-186.
- 655 Cox, G. F. N., and W. F. Weeks (1975), Brine drainage and initial salt entrapment in sodium chloride ice, *CRREL Research Report 345*, Cold Regions Research and Engineering Laboratory, Hanover, NH.
- Cox, G.F.N., and W. F. Weeks (1983), Equations for determining the gas and brine volumes in sea-ice samples, *J. Glaciol.*, 29, 306-316.
- 660 Davis, C. A. , D. R. McKenzie, and R. C. McPhedran (1991), Optical properties and microstructure of thin silver films. *Optics Comm.*, 85, 70-82.
- Deming, J. W., and H. Eicken (2007), Life in ice, in *Planets and Life: The emerging science of astrobiology*, edited by J. Baross and W. Sullivan, pp. 292-312, Cambridge University Press, Cambridge.

- 665 Dubois, M., J. J. Royer, A. Weisbrod, and A. Shtuka (1993), Reconstruction of low-  
temperature phase diagrams using a constrained least squares method: Application to  
the H<sub>2</sub>O-CsCl system, *Eur. J. Mineral.*, 5, 1145-1152.
- Eicken, H. (2003), From the Microscopic, to the Macroscopic, to the Regional Scale:  
Growth, Microstructure and Properties of Sea ice. In: *Sea Ice, An Introduction to its*  
670 *Physics, Chemistry, Biology and Geology*, edited by D.N. Thomas and G.S.  
Dieckmann, pp. 22-81, Blackwell Publishing, Oxford.
- Eicken, H., T. C. Grenfell, D. K. Perovich, J. A. Richter-Menge, and K. Frey (2004),  
Hydraulic controls of summer Arctic pack ice albedo. *J. Geophys. Res.*, 109, C08007,  
doi:10.1029/2003JC001989.
- 675 Eicken, H., C. Bock, R. Wittig, H. Miller, and H.-O. Poertner (2000), Nuclear magnetic  
resonance imaging of sea ice pore fluids: Methods and thermal evolution of pore  
microstructure. *Cold Reg. Sci. Technol.*, 31, 207-225.
- Enting, I. G. (1985), A lattice statistics model for the age distribution of air bubbles in  
polar ice, *Nature*, 315, 654-655.
- 680 Fredrich, J. T., A. A. DiGiovanni, and D. R. Noble (2006), Predicting macroscopic  
transport properties using microscopic image data. *J. Geophys. Res.*, 111, B03201,  
doi:10.1029/2005JB003774.
- Freitag, J. (1999). Untersuchungen zur Hydrologie des arktischen Meereises :  
Konsequenzen für den kleinskaligen Stofftransport (The hydraulic properties of Arctic  
685 sea-ice : implications for the small scale particle transport, in German), *Berichte zur*  
*Polarforschung (Reports on polar research)* 325, 150 pp., Ph.D. thesis, Bremen  
University.
- Freitag, J., U. Dobrindt, and S. Kipfstuhl (2002), A new method for predicting transport  
properties of polar firn with respect to gases on the pore space scale, *Ann. Glaciol.*, 35,  
690 538-544.
- Freitag J., and H. Eicken (2003), Melt water circulation and permeability of Arctic  
summer sea ice derived from hydrological field experiments, *J. Glaciol.*, 49, 349-358.
- Fredrich, J. T., A. A. DiGiovanni, and D. R. Noble (2006), Predicting macroscopic  
transport properties using microscopic image data, *J. Geophys. Res.*, 111, B03201,  
695 doi:10.1029/2005JB003774.

- Golden, K. M., S.F. Ackley, and V. I. Lytle (1998a), The percolation phase transition in sea ice, *Science*, 282, 2238-2241.
- Golden, K. M., M. Cheney, K. H. Ding, A. K. Fung, T. C. Grenfell, D. Isaacson, J. A. Kong, S. V. Nghiem, J. Sulvester, and D. P. Winebrenner (1998b), Forward  
700 electromagnetic scattering models for sea ice, *IEEE Trans. Geosci. Rem. Sens.*, 36, 1655-1674.
- Golden, K. M., D. Borup, M. Cheney, E. Cherkaeva, M. S. Sawson, K. H. Ding, A. K. Fung, Isaacson, S. A. Johnson, A. K. Jordan, J. A. Kong, R. Kwok, S. V. Nghiem, R. G. Onstott, J. Sylvester, D. P. Winebrenner, and I. H. H. Zabel (1998c), Inverse  
705 electromagnetic scattering models for sea ice, *IEEE Trans. Geosci. Rem. Sens.*, 36, 1675-1704.
- Golden, K. M., H. Eicken, A. L. Heaton, J. Miner, D. J. Pringle, and J. Zhu (2007), Thermal evolution of permeability and microstructure in sea ice, *Geophys. Res. Lett.*, 34, L16501, doi:10.1029/2007GL030447.
- 710 Hallikainen, M. , and D. P. Winebrenner (1992), The physical basis for sea ice remote sensing, in *Microwave Remote Sensing of Sea Ice, American Geophysical Union Geophys. Monogr. Ser.*, 68, edited by F. D. Carsey, 29-46, AGU, Washington, DC.
- Hunt, A. G. (2005), *Percolation Theory for Flow in Porous Media* (Lecture Notes in Physics 674), Springer, New York.
- 715 Ingham, M., D. J. Pringle, and H. Eicken (2008) Cross-borehole resistivity tomography of sea ice. *Cold Reg. Sci. Technol.*, 52, 263-277.
- Jerram, D. A., and M. D. Higgins (2007), 3D Analysis of rock textures: quantifying igneous microstructures, *Elements*, 3(4), 239-245, doi:10.2113/gselements.3.4.239.
- Ketcham, R. A., and T. Ryan (2004), Quantification and visualization of anisotropy in  
720 trabecular bone, *J. Microsc.*, 213, 158-171.
- Ketcham, R. A. (2005), Three-dimensional textural measurements using high-resolution X-ray computed tomography, *J. Struct. Geol.*, 27, 1217-1228.
- Kaempfer, T.U., M. Schneebeli, S. A. Sokratov (2005), A microstructural approach to model heat transfer in snow, *Geophys. Res. Lett.*, 32, doi:10.1029/2005GL02387.
- 725 Kawamura, T. (1986), A Method for growing large single crystals of sea ice, *J. Glaciol.*, 32, 111.

- Kawamura, T. (1998), Observations of the internal structure of sea ice by X ray computed tomography, *J. Geophys. Res.*, 93(C3), 2343 – 2350.
- 730 Krembs C., R. Gradinger, and M. Spindler (2000), Implications of brine channel geometry and surface area for the interaction of sympagic organisms in Arctic sea ice. *J. Exp. Mar. Ecol.*, 243, 55-80.
- Kusy. R. P., and D. T. Turner (1971), Electrical resistivity of a polymeric insulator containing segregated metallic particles, *Nature*, 229, 58-59.
- Krystek, M., and M. A. Anton (2007), A weighted total least-squares algorithm for fitting  
735 a straight line. *Meas. Sci. Tech.* 18, 3438, doi: 10.1088/0957-0233/18/11/025.
- Kyrylyuk, A. V., and P. van der Schoot (2008), Continuum percolation of carbon nanotubes in polymeric and colloidal media, *Proc. Natl. Acad. Sci.*, 105, 8221-8226, doi: 0.1073/pnas.0711449105.
- Lange, M.A. (1988), Basic properties of Antarctic sea ice as revealed by textural analysis  
740 of ice cores. *Ann. Glaciol.*, 10, 95–101.
- Leppäranta, M. and Manninen, T. (1988), The brine and gas content of sea ice with attention to low salinities and high temperatures: Finnish Institute of Marine Research, Internal Report 2.
- Light, B., G. A. Maykut, and T. C. Grenfell (2003), Effects of temperature on the  
745 microstructure of first-year Arctic sea ice. *J. Geophys. Res.*, 108(C2), 3050, doi: 10.1029/2001JC000887.
- Lindquist, W. B. (1999), 3DMA general users manual, SUNY-Stony Brook Tech. Rep. SUNYSB-AMS-99-20, Stony Brook Univ., Stony Brook, N. Y.
- Matsumoto, M. and T. Nishimura (1998), Mersenne Twister: A 623Dimensionally  
750 equidistributed uniform pseudorandom number generator, *ACM Trans. Mod. Comp. Sim.*, 8(1), 3-30, DOI:10.1145/272991.272995.
- Monnin, C., and M. Dubois (1999), Thermodynamics of the CsCl-H<sub>2</sub>O system at low temperatures, *Eur. J. Mineral.* 11(3), 477-482.
- Nakawo, M., and N. K. Sinha (1984), A note on brine layer spacing of first-year sea ice,  
755 *Atmosphere–Ocean*, 22(2),193–206.
- Notz, D., and M. G. Worster (2008), In situ measurements of the evolution of young sea ice, *J. Geophys. Res.*, 113, C03001, doi: 10.1029/2007JC004333.

- Patwardham, V.S., and A. Kumar (1986a), A Unified Approach for Prediction of Thermodynamic Properties of Aqueous Mixed-Electrolyte Solutions, Part 1: Vapor Pressure and Heat of Vaporization, *AIChE J.*, 32(9), 1419-1428.
- 760 Patwardham, V.S., and A. Kumar (1986b), A Unified Approach for Prediction of Thermodynamic Properties of Aqueous Mixed-Electrolyte Solutions, Part 2: Volume, Thermal, and Other Properties, *AIChE J.*, 32(9), 1429-1438.
- Perovich, D. K., and A. J. Gow (2006), A quantitative description of sea ice inclusions, *J. Geophys. Res.*, 101 (C8), 18327–18343.
- 765 Petrich, C., P. J. Langhorne, and Z. F. Sun (2006), Modelling the interrelationships between permeability, effective porosity and total porosity in sea ice. *Cold Reg. Sci. Technol.*, 44, 131-44, doi:10.1016/j.coldregions.2005.10.001.
- Pfirman, S. L., H. Eicken, D. Bauch, and W. F. Weeks (1995), The potential transport of pollutants by Arctic sea ice, *Sci. Total Env.*, 159, 129-146.
- 770 Pringle, D. J., H. Eicken, H. J. Trodahl, and L. G. E. Backstrom (2007), Thermal conductivity of landfast Antarctic and Arctic sea ice, *J. Geophys. Res.*, 112, C04017, doi:10.1029/2006JC003641.
- Prodanović, M., W. B. Lindquist and R. S. Seright (2006), Porous structure and fluid partitioning in polyethylene cores from 3D X-ray microtomographic imaging, *J. Colloid Interface Sci.*, 298, 282-297.
- 775 Roberts, J. J., J. H. Kinney, J. Siebert, and F. J. Ryerson (2007), Fe-Ni-S melt permeability in olivine: Implications for planetary core formation, *Geophys. Res. Lett.*, 34, L14306, doi:10.1029/2007GL030497.
- 780 Routh, J.E. (1905), *Dynamics of a System of Rigid Bodies*, 7<sup>th</sup> Edition, MacMillan and Co., London.
- Shklovskii, B. I., and A. L. Efros (1984), *Electronic Properties of Doped Semiconductors*, Springer-Verlag, Berlin.
- Stauffer, D., and A. Aharony (1994), *Introduction to Percolation Theory*, Taylor and Francis, London.
- 785 Thomas, D. N., and G. S. Dieckmann (2003), *Sea ice - An introduction to its physics, biology, chemistry and geology*, Blackwells Scientific Ltd., London.
- Tinga, W. R., W. A. G. Voss, and D. F. Blossey (1973), Generalized approach to multiphase dielectric mixture theory, *J. Appl. Phys.*, 44, 3897-3902.

- 790 Vancoppenolle, M., C. M. Bitz, and T. Fichefet (2007), Summer landfast sea ice  
desalination at Point Barrow, Alaska: Modeling and observations, *J. Geophys. Res.*,  
112, C04022, [doi:10.1029/2006JC003493](https://doi.org/10.1029/2006JC003493).
- Vant, M. R., R. O. Ramseier, and V. Makios (1978), The complex-dielectric constant of  
sea-ice at frequencies in the range 0.1-40 GHz, *J. Appl. Phys.*, 49, 4712-4717.
- 795 Wark, D. A., A. Williams, E. B. Watson, and J. D. Price (2003), Reassessment of pore  
shapes in microstructurally equilibrated rocks, with implications for permeability of  
the upper mantle, *J. Geophys. Res.*, 108, 10.1029/2001JB001575.
- Weeks, W.F. and Ackley, S.F. (1986), The growth, structure of sea ice, in: *The  
Geophysics of Sea Ice*, NATO ASI Series B: Physics, 146, edited by N. Untersteiner,  
800 pp. 9-164, Plenum Press, New York.
- Wettlaufer, J. S., M. G. Worster, and H. E. Huppert (2000) Solidification of leads:  
Theory, experiment, and field observations, *J. Geophys. Res.*, 105, 1123-1134.
- Yen, Y.-C. (1981), Review of thermal properties of snow, ice and sea ice, *CRREL Report*  
81-10, U. S. Army Cold Reg. Res. and Eng. Lab., Hanover, N.H.
- 805 Zhu, J., A. Jabini, K. M. Golden, H. Eicken, and M. Morris (2006), A network model for  
fluid transport in sea ice, *Ann. Glaciol.*, 44, 129 – 133.

## APPENDIX

810 **Freezing-point depression of mixed InstantOcean™-CsCl-H<sub>2</sub>O solution**

We derive the freezing-point depression for an aqueous solution mixture of InstantOcean™ and CsCl. The eutectic temperature  $T_E$  of CsCl(aq) is  $-23.7\text{ }^\circ\text{C}$  [Dubois *et al.*, 1993; Monnin and Dubois, 1999], very close to that of hydrohalite (NaCl · 2H<sub>2</sub>O) in seawater  $T_E = -22.7\text{ }^\circ\text{C}$  [Eicken, 2003]. We limit ourselves to temperatures above these, and modify the approach of Cox and Weeks [1983] and Leppäranta and Manninen [1988], both of which use the following functional forms to find the brine volume fraction,  $v_b$  :

$$v_b = (1 - v_a) \frac{\rho_i S}{F_1(T) - \rho_i S F_2(T)}, \quad (\text{A1a})$$

$$820 \quad F_1(T) = \rho_b S_b (1 + k), \quad (\text{A1b})$$

$$F_2(T) = \left( (1 + C)(\rho_b / \rho_i) - C(\rho_b / \rho_p) - 1 \right). \quad (\text{A1c})$$

Here  $i, a, b, p$  denote ice, air, brine and precipitates, respectively.  $S$  is bulk sea ice salinity and  $S_b$  is brine inclusion salinity. Two temperature-dependent precipitation coefficients are:  $k = m_{s,p} / m_{s,b}$ , the ratio of salt mass in precipitates to salt mass in brine, and  $C = m_{s,p} / m_b$ , the ratio of precipitate mass to brine mass [Cox and Weeks, 1983]. For these, we scale the values of Cox and Weeks [1983] for no CsCl precipitation.

To apply equation (A1), we need the inverse freezing-point depression relationship  $S_b(T)$  for an aqueous mixture of InstantOcean™ and CsCl. We derive this using the weighted ionic strength approach of Padwardhan and Kumar [1986a, 1986b]. The ionic strength  $\mu$  of a solute  $j$  is given by the sum over ions  $i$

$$835 \quad \mu_j = \frac{1}{2} \sum_i m_i z_i^2, \quad (\text{A2})$$

where  $m_i$  is ionic molality (mols/ liter) and  $z_i$  the integer (elementary) ionic charge. The freezing point depression  $T_\theta$  of a mixture of such solutions is then given by [Padwardhan and Kumar, 1986a, 1986b]:

$$840 \quad T_\theta = \sum_J \frac{\mu_J}{\mu_T} T_{\theta,J}(\mu_T). \quad (\text{A3})$$

Here  $J = 1$  for InstantOcean<sup>TM</sup>,  $J=2$  for CsCl, and  $T_{\theta,J}(\mu_T)$  is the freezing point depression of each solution if it had the total ionic strength of the combined solution. Ionic strength can be converted to salinity using the composition and ionic masses in InstantOcean<sup>TM</sup> and CsCl (aq). The conversion factors are:

$$\mu_{IO} [\text{molal } e^2] = 0.020028 S_{IO}[\text{ppt}], \quad (\text{A4a})$$

$$\mu_{CsCl} [\text{molal } e^2] = 0.00594 S_{CsCl}[\text{ppt}]. \quad (\text{A4b})$$

850 For InstantOcean<sup>TM</sup> we used the freezing point depression of standard seawater [Cox and Weeks, 1983] and for CsCl (aq) the result of Dubois et al. [1993]. These are fits to experimental data:

$$T_{\theta,IO} [^\circ\text{C}] = -0.5989 S - 1.142 \cdot 10^{-3} S^2 - 5.409 \cdot 10^{-4} S^3, \quad (\text{A5a})$$

$$855 \quad T_{\theta,CsCl} [^\circ\text{C}] = -0.2049 S - 4.96 \cdot 10^{-4} S^2 - 7.42 \cdot 10^{-5} S^3. \quad (\text{A5b})$$

We evaluated Equation (A3) using (A4, A5) for a 50:50 combination by weight of InstantOcean<sup>TM</sup> and CsCl. Curves fit to the results give:

$$860 \quad T_\theta [^\circ\text{C}] = -0.0403 S - 9.579 \cdot 10^{-6} S^2 - 2.31 \cdot 10^{-7} S^3, \quad (\text{A6a})$$

$$S_b [\text{ppt}] = -25.965 T - 0.7442 T^2 - 0.0107 T^3. \quad (\text{A6b})$$

Both fits have  $r^2 = 1.0$ . Finally, equation (A6b) is used in equations (1) to calculate the brine volume fraction for our samples. They are approximately 25% less than  
865 corresponding brine volumes for pure sea ice of the same salinity which is due to the

larger mass of  $\text{Cs}^+$  ions compared with common sea ice cations,  $\text{Na}^+$ ,  $\text{Mg}^{2+}$  and  $\text{K}^+$ . Equations (A6) are specific to our 50:50 % by weight mixture of InstantOcean™ and CsCl but this approach can be applied in general to similar mixtures.

870 Table 1. Target and segmented porosities. <sup>a</sup> Target porosity for  $S = 9.4 \pm 0.5$  ppt. Segmented porosities from threshold segmentation with integer threshold CT giving  $p_L$  (closest but not above  $p^*$ ) and CT + 1 giving  $p_H$  (closest, but not below  $p^*$ ). Final results were found by interpolation to  $p^*$ .

Temperature [°C]	<sup>a</sup> Target porosity $p^*$ [%]	<sup>b</sup> Integer threshold segmentation	
		$p_L$ [%]	$p_H$ [%]
-3	$11.67 \pm 0.63$	10.60	12.52
-4	$8.81 \pm 0.48$	8.17	9.60
-5	$7.12 \pm 0.38$	6.53	7.68
-6	$6.00 \pm 0.32$	5.68	6.65
-7	$5.22 \pm 0.28$	4.61	5.37
-8	$4.64 \pm 0.25$	4.02	4.84
-12	$3.06 \pm 0.16$	2.71	3.26
-15	$2.54 \pm 0.14$	2.36	2.85
-18	$2.24 \pm 0.12$	1.85	2.25

875

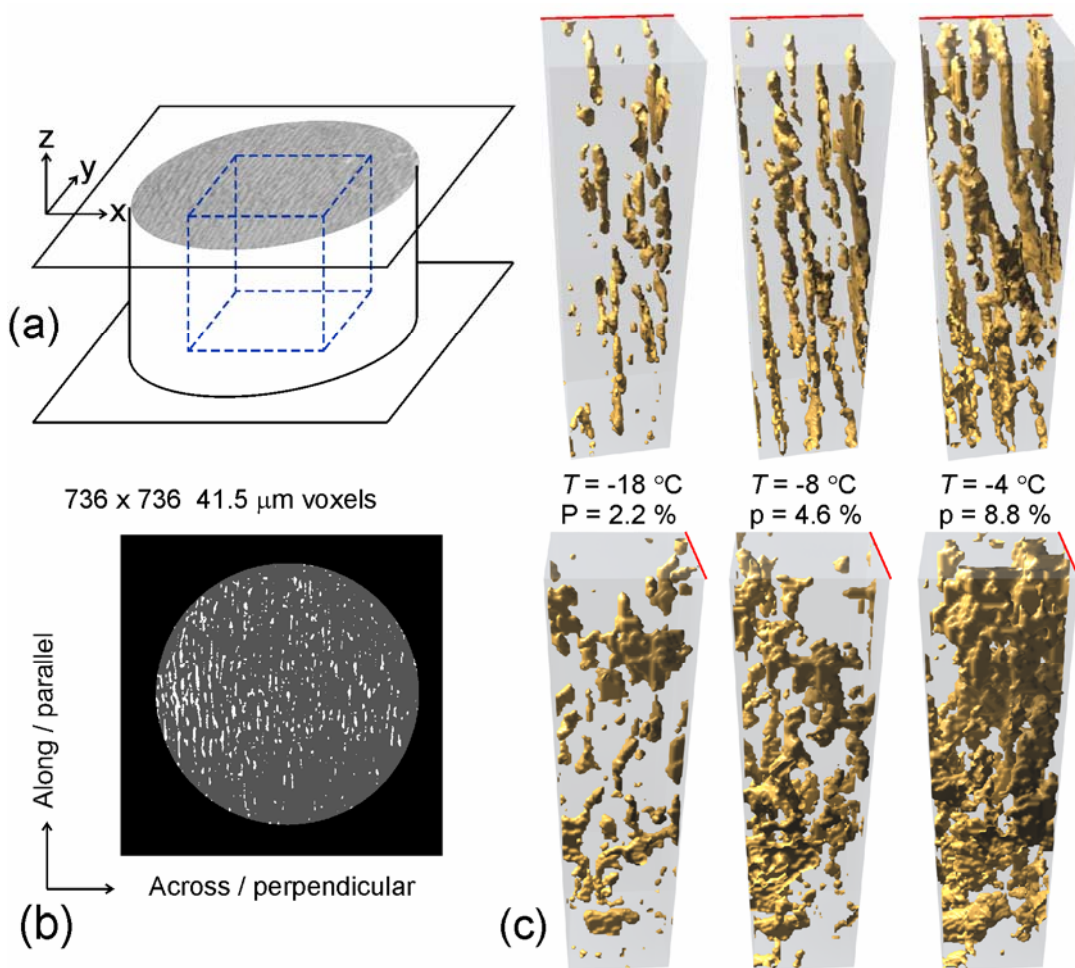
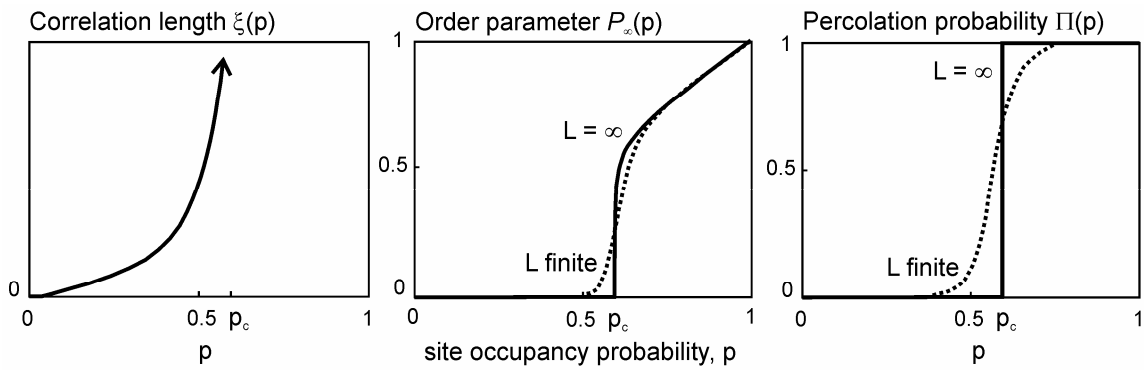


Figure 1. X-ray CT imaging of brine pore space. (a) Imaging yielded stacks of gray scale images from which connectivity was computed in sub-volumes. (b) The 3D volume was segmented into brine (white) and ice (gray). Horizontal connectivity was computed along and across brine layers after alignment with the y-axis. (c) Thermal evolution of brine pore space for nearly collocated  $50 \times 50 \times 200$  voxel sub volumes, with views of the same sub-volumes approximately along the layers (top) and across them (bottom).

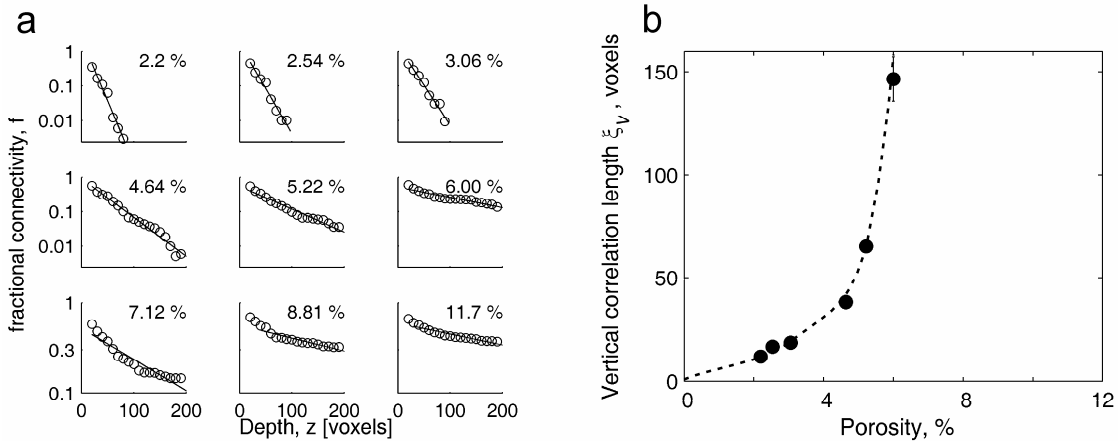
880



885

Figure 2. Key percolation functions shown for 2D site percolation, where site occupancy  $p$  is analogous to our sample porosity and  $p_c \approx 0.59$  [e.g. *Christensen and Moloney*, 2005]. Correlation length, shown only for  $p < p_c$  relevant to our work [after *Christensen and Moloney* [2005]. Order parameter results from 2D site percolation theory [Christensen and Moloney, 2005]. Percolation probability after *Stauffer and Aharony* [1994]. See text for definitions.

890



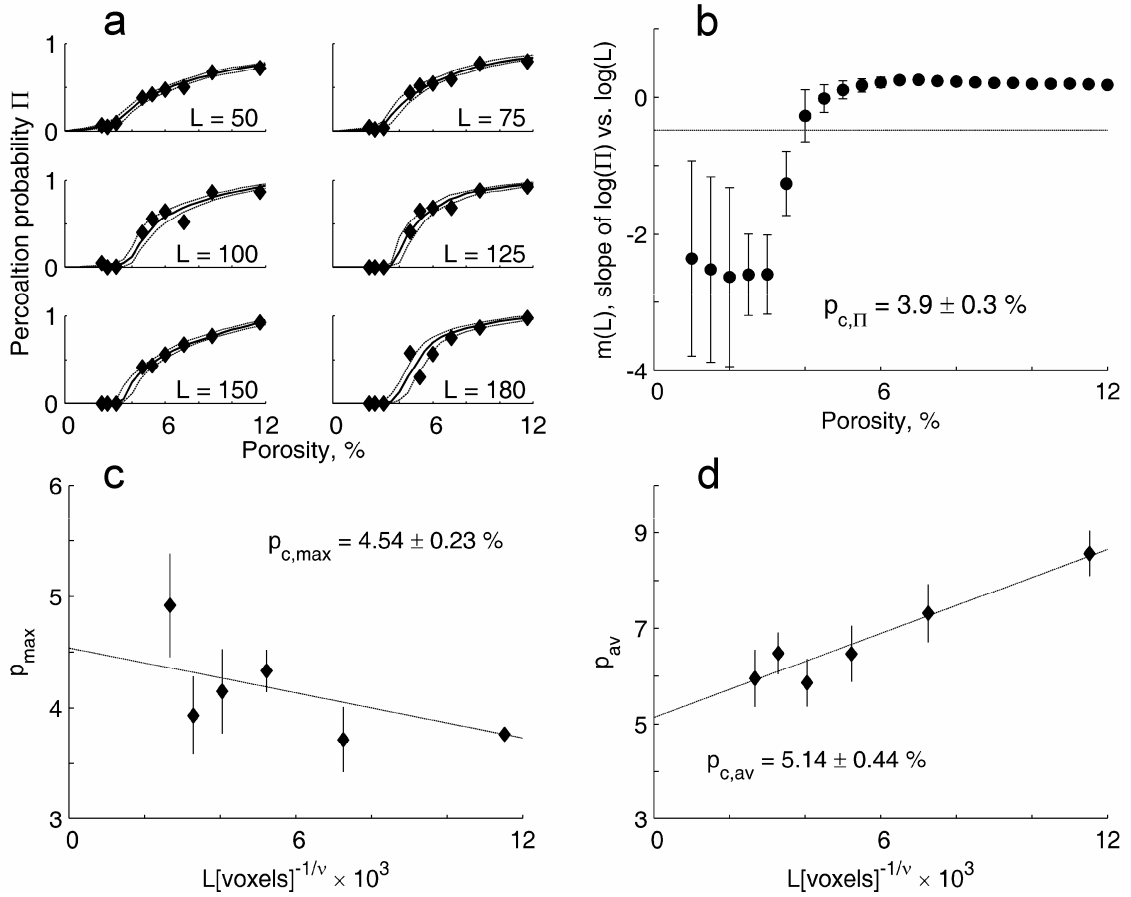
895

Figure 3. Vertical correlation length. (a) Log-linear plot of fractional connectivity vs. depth. Labels are sample porosity. Lines are fits of the form  $f(z) = C \exp(-z / z_0)$ .

Logarithmic vertical scale is the same for each row of plots; note change in bottom row.

Horizontal scale is the same in all plots. Numbers omitted for clarity. (b) Penetration

900 depth  $z_0$  for  $p \leq 6.00\%$ . Dashed line is a guide to the eye, showing divergence towards sample depth  $L = 180$  voxels.



905

Figure 4. Finite-size percolation probability  $\Pi(p,L)$ . (a) Points are computed values and lines smooth interpolations. Subplots have the same limits, omitted for clarity. (b) Calculation of  $p_c$  from power-law scaling  $\Pi(p_c,L) \propto L^{-\beta/\nu}$ . The line is  $m(L) = -\beta/\nu = -0.477$ . Finite scaling of (c)  $p_{\max}$  and (d)  $p_{\text{av}}$  with  $L^{-1/\nu}$ , where  $L$  is in units of voxels.

910 Points and error bars are the mean and standard deviations derived from the curves in (a). Lines are weighted least square fits with intercepts giving  $p_{c,\max} = 4.54 \pm 0.23 \%$  and  $p_{c,\text{av}} = 5.14 \pm 0.44 \%$ .

915

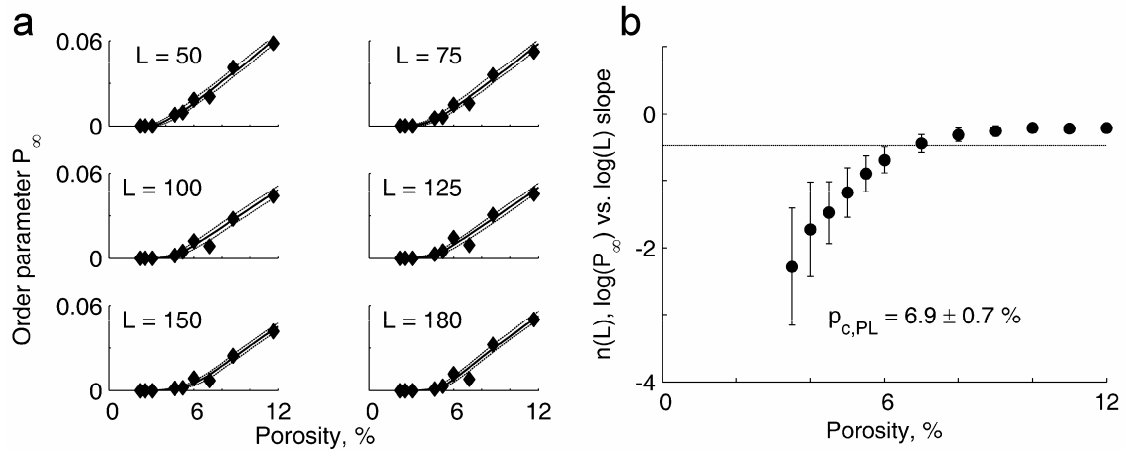


Figure 5. Order parameter  $P_\infty(p, L)$  and derived value of  $p_c$ . (a)  $P_\infty(p, L)$  points from ensemble computations where lines are interpolated fits. All subplots have the same limits, omitted for clarity. (b)  $p_c$  derived from the power-law scaling of  $P_\infty(p, L)$  with  $L$  at  $p = p_c$ . Line shows  $n(L) = -\beta/\nu = -0.477$ . Uncertainties are standard error in  $n(L)$  from weighted linear fits.

925

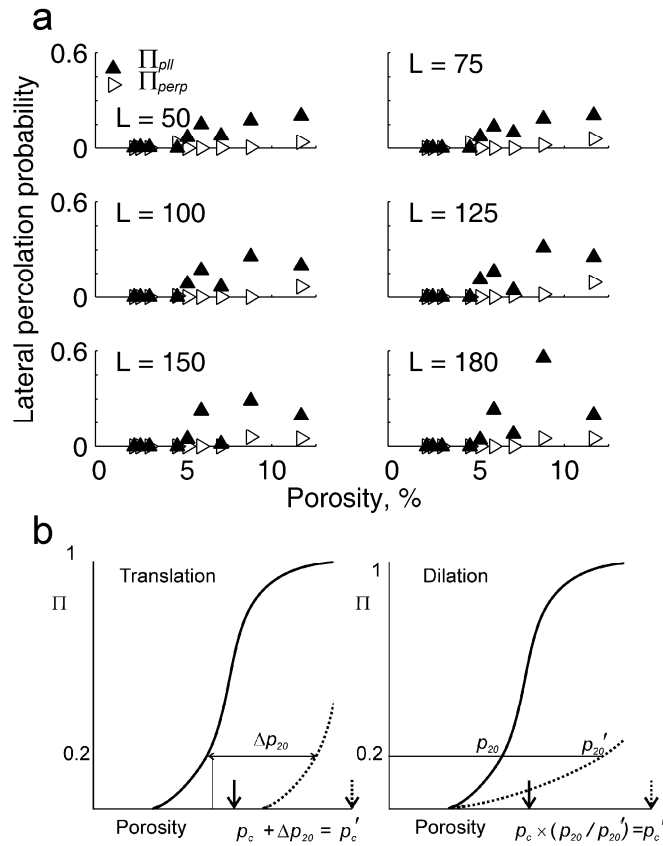


Figure 6. Horizontal percolation anisotropy. (a) Percolation probability  $\Pi_{pll}$  parallel to  
 930 brine layers, and  $\Pi_{perp}$  perpendicular to brine layers. Subplots have the same limits,  
 omitted for clarity. (b) Simple translation and dilation scaling to estimate lateral  
 thresholds  $p'_c$  from vertical  $p_c$ . Solid curves represent vertical  $\Pi(p)$  and dashed curves  
 lateral  $\Pi$ . The porosity for which  $\Pi = 0.20$  in the vertical curves is  $p_{20}$ , and for the lateral  
 curves is  $p'_{20}$ . Scaling was down for  $p_{20}$  and  $p_5$ .

935